

# Dalton Transactions

Accepted Manuscript



This is an *Accepted Manuscript*, which has been through the Royal Society of Chemistry peer review process and has been accepted for publication.

*Accepted Manuscripts* are published online shortly after acceptance, before technical editing, formatting and proof reading. Using this free service, authors can make their results available to the community, in citable form, before we publish the edited article. We will replace this *Accepted Manuscript* with the edited and formatted *Advance Article* as soon as it is available.

You can find more information about *Accepted Manuscripts* in the [Information for Authors](#).

Please note that technical editing may introduce minor changes to the text and/or graphics, which may alter content. The journal's standard [Terms & Conditions](#) and the [Ethical guidelines](#) still apply. In no event shall the Royal Society of Chemistry be held responsible for any errors or omissions in this *Accepted Manuscript* or any consequences arising from the use of any information it contains.

**Silver Intercalation in SPS dense TiS<sub>2</sub>: staging and thermoelectric properties**

*Tristan Barbier,<sup>1</sup> Oleg I. Lebedev,<sup>1</sup> Vladimir Roddatis,<sup>2</sup> Yohann Bréard,<sup>1</sup> Antoine Maignan,<sup>1</sup> and Emmanuel Guilmeau<sup>1\*</sup>*

<sup>1</sup> Laboratoire CRISMAT, UMR 6508 CNRS/ENSICAEN, 6 bd du Marechal Juin F-14050

CAEN Cedex 4, France

<sup>2</sup> CIC energiGUNE, Albert Einstein 48, 01510 Miñano, Alava, Spain

**Abstract**

Polycrystalline samples in the series Ag<sub>x</sub>TiS<sub>2</sub> with  $x$  varying from 0 to 0.2 were prepared using solid-liquid-vapor reaction and Spark Plasma Sintering. Depending on the  $x$  content, it is found that different staging can occur with intercalation, from the so-called 1T-TiS<sub>2</sub> (stage 1) to ordered Ag<sub>1/6</sub>TiS<sub>2</sub> (stage 2). Randomly intercalated Ag cations in the Van der Waals gap of stage 1 and stage 2 based TiS<sub>2</sub> structure induce a strong decrease of lattice thermal conductivity through structural disorder. Decrease in electrical resistivity and absolute value of the Seebeck coefficient with increasing Ag content supports also the charge transfer to the Ti 3d conduction band, enhancing the power factor in specific temperature range. Thus, the combined effects of Ag intercalation are beneficial to the improvement in ZT, reaching around 0.45 at 700K in Ag intercalated compounds.

---

\* Corresponding Author: [emmanuel.guilmeau@ensicaen.fr](mailto:emmanuel.guilmeau@ensicaen.fr)

## 1. Introduction

In recent years, thermoelectric materials have been intensively explored for possible applications to electric-power generators due to their capacity to directly convert the waste-heat into electricity. Their performances are evaluated by the dimensionless thermoelectric figure of merit  $ZT = \frac{S^2}{\rho\kappa}T$ , where  $S$  is the Seebeck coefficient,  $\rho$  is the electrical resistivity,  $\kappa$  is the thermal conductivity and  $T$  the absolute temperature. For applications below 600 K, best performances are obtained by  $\text{Bi}_2\text{Te}_3$  with optimum  $ZT$  values around 1 (or even higher) at 400 K [1]. However, due to the tellurium toxicity, scarcity and cost, these bulk thermoelectric materials cannot be used for large scale applications.

Several studies have recently shown that  $\text{TiS}_2$  is an attractive substitute as its power factor values [2 – 7] are close to those of bismuth telluride [1].  $\text{TiS}_2$  is a member of the large family formed by the layered transition metal dichalcogenides  $\text{TX}_2$  [8] ( $T$  = transition metal; and  $X$  = chalcogenide). Structurally,  $1\text{T-TiS}_2$  is built by  $\text{CdI}_2$ -type layers which are bonded by Van der Waals forces. Intercalation in  $\text{TiS}_2$  is also known and the presence of intercalants in the Van der Waals gap is a way to control the doping in the  $\text{TiS}_2$  slabs by charge transfer. Also, the presence of these intercalated species has been shown to be efficient in order to reduce the lattice part of the thermal conductivity as in the case of  $\text{Cu}_x\text{TiS}_2$  [3]. A similar effect on the thermal conductivity was first reported in the case of the “misfit”  $(\text{MS})_{1+x}(\text{TiS}_2)_2$  ( $M = \text{Pb}, \text{Bi}, \text{Sn}$ ) [4].

An overview of the  $\text{M}_x\text{TiS}_2$  intercalation (**Fig. 1b and 1c**) in  $\text{TiS}_2$  (**Fig. 1a**), where  $M$  is a metal, reveals that it operates through two types of mechanism [9]. A continuous variable content of  $x$  intercalates randomly distributed over every layer interspacing in the so-called stage 1 structure of  $\text{TiS}_2$  (**Fig. 1b**) or by staging leading to the formation of a

superstructure, as in the case of  $\text{Ag}_{1/6}\text{TiS}_2$  [10], which stage 2 structure (**Fig. 1c**) can be described as a 1:1 ordering of empty and 1/3 filled Van der Waals gaps. Accordingly, for  $x < 1/6$  in  $\text{Ag}_x\text{TiS}_2$ , the intercalation produces a mixture, at the microscopic scale, of stage 1 and stage 2 phases, whereas for  $x > 1/6$ , it creates a long-range mixture made of stage 2 phase with an Ag-rich stage 1 phase [11]. Up to now, the synthesis of these intercalated  $\text{TiS}_2$  samples was made by heating  $\text{TiS}_2$  and Ag powders in evacuated ampoules. In the present paper, in order to obtain dense materials, the pre-reacted  $\text{Ag}_x\text{TiS}_2$  powders have been densified by spark plasma sintering (SPS). The structural properties of the obtained pucks have been characterized by powder X-Ray Diffraction (XRD) and Transmission Electron Microscopy (TEM) (Electron Diffraction (ED) and High Resolution TEM (HRTEM)). They show staging effects in “SPS”  $\text{Ag}_x\text{TiS}_2$  samples as in the classical route. The obtained physical properties demonstrate that the lattice part of the thermal conductivity of these dense samples ( $> 95\%$ ) can be strongly reduced as compared to that of the pristine  $\text{TiS}_2$  compound processed by the same sintering method. At 700 K,  $ZT = 0.42 - 0.46$  values were reached for materials of starting compositions  $\text{Ag}_x\text{TiS}_2$  with  $0.02 \leq x \leq 0.10$ .

## 2. Experimental Section

### 2.1. Synthesis

$\text{Ag}_x\text{TiS}_2$  dense ceramics were synthesized in a two steps process. First,  $\text{Ag}_x\text{TiS}_2$  powders were synthesized (in sealed fused silica tube at 923 K for 12 h) by solid-liquid-vapor reaction from the stoichiometric mixture of pure elements (325 Mesh, Alfa Aesar 99.5 %). The resulting agglomerated powder, composed of plate-like grains of 1 - 5  $\mu\text{m}$  (in the  $ab$  plane), was then ground and sieved down to 200  $\mu\text{m}$  to remove large agglomerates.

Secondly, the powders were placed in graphite dies of 15 mm diameter and densified by Spark Plasma Sintering (SPS) (FCT HPD 25) at 1023 K for 30 min under vacuum (heating and cooling rate of 100 K/min) under a uniaxial pressure of 50 MPa.

. The final dimensions of each pellet are around 7 mm in thickness and 15 mm in diameter. The densities of all these compounds were higher than 95 % of the theoretical one.

## 2.2. X-ray Diffraction

Powder diffraction data for Rietveld refinements were collected using a D8 Advance Vario 1 Bruker diffractometer (Bragg-Brentano mode) with Lynx Eye detector with a Ge (111) monochromator (Johansson type) using the Cu radiation ( $\lambda = 1.545982 \text{ \AA}$ ). X-Ray Diffraction (XRD) data were collected from 5 to 120 ° with a step size of 0.011°, and a step time of 2 s.

A diffraction pattern of a standard LaB<sub>6</sub> powder was also registered under the same conditions in order to obtain the instrumental broadening of the diffractometer. The angular dependence of the Full Width at Half Maximum (FWHM) of the diffraction peak obtained for this standard was chosen as Caglioti type [FWHM ( $\theta$ ) = (U tan<sup>2</sup>  $\theta$  + V tan  $\theta$  + W)<sup>1/2</sup>], where U, V and W are refinable parameters [12]. The resulting Lorentzian and Gaussian FWHM were added to the instrumental parameters file (Instrumental Resolution Function: \*.irf file).

The full-profile-fitting refinements were carried out by the Rietveld method, using the *Fullprof* program [13]. The peak shape was corrected from the instrumental broadening using the aforementioned \*.irf file and then modelled with the TCH pseudo-voigt profile function (NPR = 7) [14] with a mixing parameter depending on the microstructure of the powdered sample. For the structure refinement, the systematic error corrections (zero-point

shift and asymmetry) were applied and the background was adjusted using a polynomial function of 24 degrees. With respect to the crystallographic structure, the lattice parameters, atomic positions and isothermal temperature factor ( $B_{iso}$ ) were also refined (occupancy of all atoms were fixed to 1).

At first, all the Rietveld modellings were performed with an isotropic crystallite size. This is illustrated by  $Ag_{0.05}TiS_2$ . However it has been observed on each diagram the following mistakes on the calculation peaks shape (**Fig. 2**):

- For the peaks where  $h, k > l$ , it can be observed that the calculated Full Widths at Half Maximum (FWHM) are larger, and the intensities are lower than the experimental data.
- For the peaks where  $h, k < l$ , it can be also observed that the calculated FWHM are lower and the intensities are larger than the experimental data.

In order to understand these phenomena, scanning electron microscopy (SEM, Zeiss Supra 45) analyses were performed on each densified samples. It has been observed that the main part of grains is platelet-like shape. This data was also confirmed by TEM. So, modelling with an anisotropic crystallite sizes (vector  $(00l)$ ;  $lorsize = l$  in Fullprof software) have been performed on each diagram. The resulting modelling leads to a better fitting of peak shape (**Fig. 2**) and a significant decrease of the reliability factors, as it can be observed through the blue lines on the **Figure 2**, showing the difference between the experimental data and the calculated ones. This indicates that the crystallite/grain shape must be taken into account in the present compounds for a better refinement of the experimental data. Crystallographic parameters, percentage for each phase of nominal composition " $Ag_xTiS_2$ ", (**Table 1**) were determined using this modelling approach. The refined XRD pattern is presented in

**Figure 3.**

### 2.3. Electron Microscopy

Transmission electron microscopy (TEM) including high resolution TEM (HRTEM) and electron diffraction (ED) studies were performed using a Tecnai G2 30 UT (LaB<sub>6</sub>) microscope operated at 300 kV, having 0.17 nm point resolution and equipped with EDAX EDX detector. High Angle Annular Dark Field (HAADF) and scanning TEM (STEM) studies were performed using a Tecnai F20 (FEG) electron microscopes operated at 200 kV. Samples for TEM analyses were prepared in two different ways. A part of the sample was ground under ethanol and the resulting dispersion was transferred to a lacey or holey carbon film fixed on a 3 mm copper grid. In a second approach, the samples were polished mechanically down to 20  $\mu\text{m}$  thicknesses following by ion Ar<sup>+</sup> ion milling with the energy 3 kV until the perforation using Fischione 1010 Ion Mill.

### 2.4. Thermoelectric and Electronic Measurements

The electrical resistivity ( $\rho$ ) and Seebeck coefficient (S) were measured simultaneously in the temperature range of 300 - 700 K using a ULVAC-ZEM3 device under partial helium pressure. The heat capacity and thermal diffusivity were analysed using a Netzsch DSC 404C and a LFA-457 model, respectively. The total thermal conductivity ( $\kappa_{\text{total}}$ ) was determined by using the product of the geometrical density, the thermal diffusivity and the heat capacity. Lattice thermal conductivity ( $\kappa_l$ ), was calculated by subtracting the electronic contribution (Lorenz number of  $2.45 \cdot 10^{-8} \text{ W} \cdot \Omega \cdot \text{K}^{-2}$ ) to the total thermal conductivity ( $\kappa_{\text{total}}$ ).

The Hall effect experiments have been carried out in a physical Properties Measurements Systems (PPMS, Quantum Design), in a magnetic field up to 7 Tesla.

All the property measurements were performed on the same puck. Scanning electron microscopy and XRD revealed a weak preferential crystallographic orientation of the obtained pellets with the stacking direction (*c* axis) along the applied pressure direction [15]. Accordingly, the measurements of *S*,  $\rho$  and  $\kappa$  were all performed along the average (*ab*) planes of the sample.

### 3. Results and Discussion

#### 3.1. Structural analysis by X-ray and electron diffraction

As mentioned in the introduction, the  $\text{Ag}^+$  intercalation in  $\text{TiS}_2$  by heating stoichiometric amounts of Ag and  $\text{TiS}_2$  powder in close ampoule at high temperature (800 °C and 1000 °C in ref. [11]) induces, for  $0.02 \leq x \leq 0.18$  in  $\text{Ag}_x\text{TiS}_2$ , a mixture between a phase derived from the stage 1, 1T- $\text{TiS}_2$  and another one derived from the stage 2,  $\text{Ag}_{1/6}\text{TiS}_2$ .

First, in order to test the possibility to obtain a dense stage 2 phase by SPS, a compound of nominal composition  $\text{Ag}_{0.2}\text{TiS}_2$  was sintered. The corresponding room temperature XRD pattern, fitted by combining stage 1 and stage 2 phases (see tick marks in **Figure 4b**), reveals a majority of stage 2 phase with unit cell parameters  $\mathbf{a} = 3.416(1) \text{ \AA}$  and  $\mathbf{c} = 12.110(1) \text{ \AA}$  in the  $\text{P}\bar{3}\text{m}1$  space group (**Table 2**). A very good agreement with the values reported for the  $\text{Ag}_{1/6}\text{TiS}_2$  thermally intercalated stage 2 phase (ICSD reference #68865  $\mathbf{a} = 3.1416 \text{ \AA}$  and  $\mathbf{c} = 12.100(1) \text{ \AA}$  for  $\text{Ag}_{1/6}\text{TiS}_2$ ) is observed. This majority phase is coexisting with a minority stage 1 phase of unit cell parameters  $\mathbf{a} = 3.417(5) \text{ \AA}$  and  $\mathbf{c} = 6.023(4) \text{ \AA}$  ( $\text{P}\bar{3}\text{m}1$  space group, **Table 2**). The latter  $\mathbf{a}$  and  $\mathbf{c}$  parameters larger than  $\mathbf{a} = 3.4073 \text{ \AA}$  and  $\mathbf{c}$

= 5.6953 Å for  $\text{TiS}_2$  (ICSD reference #52195) strongly supports that some  $\text{Ag}^+$  cations are also intercalated in the stage 1  $\text{TiS}_2$  phase as also observed in ref. [11] for a  $\text{Ag}^+$  nominal content corresponding to  $x = 0.2$ . Also not very precise, the estimated phase wt.% fraction obtained from these refinements leads to 85 wt.% of stage 2  $\text{Ag}_{1/6}\text{TiS}_2$  and 15 wt.% of stage 1  $\text{Ag}_x\text{TiS}_2$ .

These results demonstrate that the stage 2  $\text{Ag}_{1/6}\text{TiS}_2$  phase can be also stabilized by SPS. Nonetheless, they show that the material is not homogeneous and should be rather considered as a composite to interpret the thermoelectric performances described in the following section.

The presence of the stage 2 phase was also confirmed by ED studies (**Fig. 4a**), which shows extra peaks along the [001] direction (right pattern in Fig. 4a) corresponding to a doubling of the c-parameter as compared to stage 1. When the doubling is observed, the EDS analysis leads to a silver content close to  $x = 0.15$  which is in good agreement with the expectations.

Taking into consideration that the best performances in the  $\text{Cu}_x\text{TiS}_2$  series are evidenced for only small  $x$  values with an optimum at  $x = 0.04$  [3], other  $\text{Ag}_x\text{TiS}_2$  samples were prepared for  $x \leq 0.10$  values ( $x = 0, 0.02, 0.05, 0.1$ ). The XRD patterns collected at room temperature are given in **Fig. 5**. Starting from  $x = 0.1$ , by comparing with the  $x = 0.2$  pattern, it is obvious that the compound of nominal composition “ $\text{Ag}_{0.1}\text{TiS}_2$ ” contains a mixture of two phases, a stage 1 and a stage 2 one. But for this composite, the  $c$  axis of the stage 1 phase is smaller (5.7267(8) Å against 6.0234(8) Å for stage 1 in the “ $\text{Ag}_{0.2}\text{TiS}_2$ ” composite) which indicates that the Ag content is smaller. A similar conclusion is obtained for the stage 2 phase (11.7630(2) Å against 12.1094(2) Å) which could indicate that Ag is missing to

fulfill all the octahedral sites of the ideal stage 2 compositions  $\text{Ag}_{1/6}\text{TiS}_2$ . However, the weight fractions of the two constitutive phases obtained from the refinements in “ $\text{Ag}_{0.1}\text{TiS}_2$ ” are opposite to those obtained for in “ $\text{Ag}_{0.2}\text{TiS}_2$ ”, with a majority of stage 1 Ag intercalated  $\text{TiS}_2$  (92 % against only 8 % of stage 2  $\text{Ag}_x\text{TiS}_2$ ). This result could be explained by the model given by Bardhan *et al.* [11] where these phases are supposed to coexist at the microscopic level. As  $x$  decreases from  $x = 1/6$ , the volume of the stage 2 is expected to decrease as  $x$  deviates more and more. This is consistent with the unit cell  $c$  (or  $c/2$ ) parameters of both phases- stage 1 and stage 2 - which both increase as  $x$  increases from  $x = 0.02$  to  $x = 0.1$  (**Table 1**). From transmission electron microscopy, for these  $x$  values, mainly the stage 1 can be observed as seen from the ED patterns for the  $x = 0.05$  sample (see the [001] and [010] patterns in **Fig. 6a**) and from the corresponding HRTEM images (**Fig. 6b and 6c**). This is consistent with a disordering in the intercalated layers, which precludes evidencing a neat co-existence of stage 1 and stage 2 forms.

Nevertheless, the high resolution imaging and electron diffraction study of the “ $\text{Ag}_{0.1}\text{TiS}_2$ ” ( $x = 0.1$ ) sample support the existence of local disordering related to local deviation of the Ag content in between successive  $\text{TiS}_2$  slabs (**Fig. 7**). HRTEM image demonstrates the disordered character of the structure. The clear “wavy” structure is caused by the mixture of stage 1 and locally short range stage 2 structures.

The presence of streaks on the main spots in the [010] electron diffraction pattern (**Fig. 7**) indicates the presence of stacking faults. The elongations of the (001) spots are consistent with local variations of the  $c$  axis values as a result of the closeness of the  $c$  parameter for the stage 1 and  $c/2$  for the stage 2 phase. It supports that the distance between two successive layers is spontaneously increased or decreased, which confirms that the silver cations are randomly distributed in the  $\text{TiS}_2$  host structure.

To sum-up, this structural part demonstrates a similar non continuous intercalation with  $x$  in  $\text{Ag}_x\text{TiS}_2$  for samples prepared either by SPS or by classical thermal treatment. For the stage 2 phase in “ $\text{Ag}_{0.2}\text{TiS}_2$ ” at room temperature, no in plane super structure according to a  $\sqrt{3}x\sqrt{3}$  R30° 2D ordering is observed as expected from the fact that this order-disorder transition (for that silver nominal content) is expected to be below, at  $T = 270 \text{ K} - 280 \text{ K}$  [16] (**Fig. 4a**, left pattern).

Finally, for the highest silver content ( $x = 0.2$ ), the local change in the silver intercalated amount can even lead to defective regions as shown in **Fig. 8**. The bending of the  $\text{TiS}_2$  layers is evidenced by the HRTEM (**Fig. 8c**) image and HAADF-STEM images (**Fig. 8a**) and also splitting of the  $\text{TiS}_2$  layers and formation of amorphous regions. EDX profiling (**Fig. 8a insert**) also shows inhomogeneous distribution of Ag cations in the  $\text{TiS}_2$  matrix. Some other very rare defects are detected as shown in this figure: locally a thin layer made of about two planes of Ag metal is evidenced (**Fig. 8b**). Such a defect could impact the transport properties as they could shortcut the electrical current. However, their origin is unclear: they could result from some Ag migration under the electron beam of the TEM or from thermally activated silver migration during SPS, or even at room temperature, as already mentioned for these materials known to be ionic conductors [17].

The coexistence induced by staging of different phases for the present SPS  $\text{Ag}_x\text{TiS}_2$  samples differs from the monophasic character of other  $\text{M}_x\text{TiS}_2$  series ( $M = \text{Cu}, \text{Nd}, \text{Bi}$ ) characterized by a continuous intercalation process [3, 17, 18]. The corresponding disorder should be favorable for the reduction of the lattice part of the thermal conductivity.

### 3.3. Thermoelectric properties

The temperature dependences of the electrical resistivity ( $\rho$ ) and Seebeck coefficient ( $S$ ) in the  $\text{Ag}_x\text{TiS}_2$  series are displayed in **Figure 9**. The data were collected from 300 K to 700 K. The values obtained for the pristine material (*i.e.*  $\rho = 1.63 \text{ m}\Omega\cdot\text{cm}$ ,  $S = -153 \text{ }\mu\text{V/K}$  @ 300K for  $x = 0$ ) are quite similar to those obtained by Guilmeau *et al.* [3] for  $x = 0$  in the  $\text{Cu}_x\text{TiS}_2$  series (*e.g.*  $\rho = 1.55 \text{ m}\Omega\cdot\text{cm}$ ,  $S = -155 \text{ }\mu\text{V/K}$ , for  $\text{TiS}_2$ ), despite a lower sintering temperature was used during SPS in the former (*i.e.*  $750 \text{ }^\circ\text{C}$  against  $900 \text{ }^\circ\text{C}$ ). As  $x$  increases in  $\text{Ag}_x\text{TiS}_2$ , it is found that the  $\rho$  and  $|S|$  values decrease, showing that  $n$ -type charge carriers ( $S < 0$ ) are created by the Ag intercalation. They reach  $\rho = 0.4 \text{ m}\Omega\cdot\text{cm}$  and  $|S| = 30 \text{ }\mu\text{V/K}$  for “ $\text{Ag}_{0.2}\text{TiS}_2$ ”. Hall effect measurements confirm an electron concentration  $n$  of  $7.4 \times 10^{20} \text{ cm}^{-3}$  for  $x = 0$  which can be well compared to those reported previously in  $\text{TiS}_2$  crystal ( $n = 6.7 \times 10^{20} \text{ cm}^{-3}$ ) and bulk polycrystals ( $6.5 \times 10^{20} \text{ cm}^{-3}$ ) [2, 3]. The presence of random Ti intercalation in  $\text{TiS}_2$ , as suggested by the increase in  $c$  parameter in the  $\text{TiS}_2$  phase ( $x = 0$ ), explains the carrier concentration increase. According to the composite nature of the other members in the series ( $x = 0.02, 0.05, 0.1$ ), no Hall measurements were performed.

The temperature dependence of the power factor ( $\text{PF} = S^2/\rho$ ) evolves with the silver content (**Fig. 10**). Whereas the two first members ( $x = 0, 0.02$ ) exhibit a negative temperature dependence, the magnitude of PF remains relatively constant around  $1 \text{ mW/mK}^2$  on the full temperature range for  $x = 0.05$ . For  $\text{TiS}_2$ , the power factor is equal to  $1.5 \text{ mW/mK}^2$  at 300 K which is slightly smaller than the value reported previously in  $\text{Cu}_x\text{TiS}_2$  (*i.e.*  $1.7 \text{ mW/mK}^2$  for  $x = 0.00$  [3]). Such small difference most probably originates from the difference in sintering temperature ( $750 \text{ }^\circ\text{C}$  against  $900 \text{ }^\circ\text{C}$  in  $\text{Cu}_x\text{TiS}_2$ ), which induces slight difference in transport properties due to different grain size and/or small variation in the Ti/S ratio. On

the other hand, the  $\text{Ag}_{0.02}\text{TiS}_2$  compound exhibits improved power factor compared to  $\text{TiS}_2$  for the full temperature range, varying from  $1.5 \text{ mW/mK}^2$  (300 K) to  $1.1 \text{ mW/mK}^2$  (700 K). The temperature dependence and magnitude of PF is also rather similar to  $\text{Cu}_{0.02}\text{TiS}_2$  [3]. This demonstrates that, though the Ag intercalation mechanism by staging differs from the continuous intercalation in  $\text{Cu}_x\text{TiS}_2$ , the similar evolution of both  $\rho$  and  $S$  with  $x$  reflects that the charge creation is monotonous with  $x$  up to  $x = 0.1$ .

In principle, the presence of silver in the intercalation sites should deteriorate the lattice part of the thermal conductivity. The temperature dependences of the thermal conductivity ( $\kappa$ ) and lattice component ( $\kappa_l$ ) in **Fig. 11** show that  $\kappa$  remains constant with  $x$  content increase. As the electronic contribution ( $\kappa_e$ ) of  $\kappa$  increases with  $x$  due to charge carriers doping, thus, this increase must be compensated by a decrease of  $\kappa_l$  as shown in **Fig. 11**.  $\kappa$  for the  $\text{TiS}_2$  pristine compound ( $x = 0$ ) has a different temperature dependence with comparable or higher  $\kappa$  values (especially over 450 K) to those of the Ag intercalated compounds. This difference between “ $\text{Ti}_{1+x}\text{S}_2$ ” and “ $\text{Ag}_x\text{TiS}_2$ ” can be ascribed to the mass difference between the intercalants (Ti or Ag) and the host ions in the conducting layers (Ti and S). Although the Ag intercalation mechanism by staging differs from that with other metal such as Cu, the decrease in  $\kappa_l$  as the silver content increases is rather similar: at 700 K,  $\kappa_l = 0.9 \text{ W/mK}$  in  $\text{Ag}_{0.1}\text{TiS}_2$  against  $\kappa_l = 0.8 \text{ W/mK}$  for  $\text{Cu}_{0.1}\text{TiS}_2$  [3].

The temperature dependence of the dimensionless figure of merit  $ZT$  of the  $\text{Ag}_x\text{TiS}_2$  series is given in **Fig. 12**. The  $ZT$  value for all specimens increases with increasing temperature. The  $ZT$  value of  $\text{Ag}_{0.02}\text{TiS}_2$  is slightly increased compared with  $\text{TiS}_2$ , whereas for  $x = 0.05$  and  $x = 0.10$  intercalated compounds it tends to exhibit lower values below 450 K. Above 450 K, the Ag intercalated compounds exhibit improved  $ZT$  values as compared to  $\text{TiS}_2$

with a maximum around 0.45 at 700 K for the three members of the series ( $x = 0.02, 0.05$  and 0.10).

#### 4. Conclusion

This study shows that randomly intercalated Ag cations in the Van der Waals gap of stage 1 and stage 2 based  $\text{TiS}_2$  structure are highly effective to reduce the lattice thermal conductivity through structural disorder. Also, silver intercalation provides additional carriers (electrons) through charge transfer to the Ti 3d conduction band to tune the carrier concentration enhancing the power factor in specific temperature range. These peculiar features of the Ag intercalation are responsible for the ZT improvement, reaching around  $ZT=0.45$  at 700K. This study supports the concept that layered based compounds are ideal candidates to create structural lattices where both electrical and thermal properties can be improved by cation intercalation and/or substitution. Finally, as ionic conductivity precludes the use of materials in thermoelectric devices, we must determine if the present Ag-intercalated compounds with small  $x$  contents are ionic conductors or not.

**References:**

1. T. M. Tritt and M. A. Subramanian, *MRS Bulletin*, 31 (2006).
2. H. Imai, Y. Shimakawa, Y. Kubo, *Phys. Rev. B*. 64 (2011) 241104.
3. E. Guilmeau, Y. Bréard and A. Maignan, *Appl. Phys. Lett.* 99 (2011) 052107.
4. K. Koumoto, R. Funahashi, E. Guilmeau, Y. Miyazaki, A. Weidenkaff, Y.F. Wang, C.L. Wan, *J. Amer. Ceram. Soc.* 96 (2013) 1-23.
5. S. Hébert, W. Kobayashi, H. Muguerra, Y. Bréard, R. Nunna, F. Gascoin, E. Guilmeau and A. Maignan, *Phys. Status Sol. A- Applications and Materials Science* 210 (2013) 69-81.
6. M. Beaumale, T. Barbier, Y. Bréard, G. Guelou, A.V. Powell, P. Vaquero, E. Guilmeau, *Acta Materialia* 78 (2014) 86
7. M. Ohta, S. Satoh, T. Kuzuya, S. Hirai, M. Kunii, A. Yamamoto, *Acta Materialia*, 60 (2012) 7232-7240.
8. J.A. Wilson and A.D. Yoffe, *Advances in Physics* 18:73 (1969) 193.
9. A. Saxena and J.D. Gunton, *Acta Cryst.* A42 (1986) 399.
10. G. A. Scholz, R. F. Frindt, *Mater. Res. Bull.* 15 (1980) 1703-1716.
11. K.K. Bardan, G. Kirczenow, G. Jackle and J.C. Irwin, *Phys. Rev. B* 33 (1986) 4149.
12. G. Caglioti, A. Paoletti and F.P. Ricci, *Nuclear Instrument*, 3 (1958) 223-228.
13. J. Rodriguez-Carvajal, *Physica B*, 55 (1993) 192.
14. Thompson, Cox and Hastings, *J. Appl. Cryst.* 20, 79 (1987).
15. M. Beaumale, T. Barbier, Y. Breard, S. Hebert, Y. Kinemuchi, and E. Guilmeau, *J. Appl. Phys.* 115 (2014) 043704.
16. G.A. Jackle and J.C. Irwin, *J. Phys. C: Solid State Phys.* 21 (1988) 17.

17. A.N. Titov, Physics of the Solid State 51 (2009) 714.

**Figure Captions:**

**Figure 1:** Schematic representations of a)  $\text{TiS}_2$ , b)  $\text{Ag}_x\text{TiS}_2$ , stage 1 and c)  $\text{Ag}_{0.167}\text{TiS}_2$ , stage 2.

**Figure 2:** Effect of the anisotropic modelisation (bottom panel) compared to isotropic (top panel) on the powder X-Ray diffraction pattern of the “ $\text{Ag}_{0.05}\text{TiS}_2$ ” compound.

**Figure 3:** Powder X-ray diffraction pattern of  $\text{Ag}_{0.05}\text{TiS}_2$ ; the upper Bragg positions between the observed pattern and the difference profile correspond to the stage 1  $\text{Ag}_x\text{TiS}_2$  and lower marks correspond to the stage 2  $\text{Ag}_{0.167}\text{TiS}_2$ . Observed (red solid lines) and calculated (black circles) data. The difference profile is shown at the bottom (blue solid lines).

**Figure 4:** a) ED patterns of  $\text{Ag}_{0.2}\text{TiS}_2$  taken along [001] and [010] zone axis, b) Powder X-ray diffraction pattern of the “ $\text{Ag}_{0.2}\text{TiS}_2$ ” composite; the upper Bragg positions between the observed pattern and the difference profile correspond to the stage 1  $\text{Ag}_x\text{TiS}_2$  phase and the lower marks correspond to stage 2  $\text{Ag}_x\text{TiS}_2$ . Observed (red solid lines) and calculated (black circles) data. The difference profile is shown at the bottom (blue solid lines).

**Figure 5:** Experimental powder X-ray diffraction patterns of  $\text{Ag}_x\text{TiS}_2$  with  $x = 0; 0.02; 0.05; 0.1; 0.2$  (left panel) and corresponding enlargements in the  $28^\circ$  to  $40^\circ$  region. The # denotes some traces of  $\text{Ag}_2\text{S}$  which crystallizes in the  $\text{P}2_1/\text{c}$  ( $n^\circ 14$ ) space group.

**Figure 6:** a) ED patterns of  $\text{Ag}_{0.05}\text{TiS}_2$  taken along [001] and [010] zone axis, b)[010] HRTEM and (c) - high resolution HAADF STEM images of  $\text{Ag}_{0.05}\text{TiS}_2$  structure.

**Figure 7:** [010] HRTEM image of “ $\text{Ag}_{0.1}\text{TiS}_2$ ” sample. Local incorporation of stage 2 structure in form of defects is marked with white arrows. The [010] ED pattern is given as an inset.

**Figure 8:** (a) – Low magnification HAADF-STEM image of the “Ag<sub>0.2</sub>TiS<sub>2</sub>” sample and line EDX scan profile. Enlargement shows elemental profile along scan line (in red) for Ti (green), S(red) and Ag(blue). Notice the Ag varying within the single grain. (b) High resolution HAADF-STEM image of atomically thin Ag layer in TiS<sub>2</sub> matrix.(c) HRTEM image of the “Ag<sub>0.2</sub>TiS<sub>2</sub>” sample. Stacking faults are marked with white arrows. The bending of layers is clearly seen.

**Figure 9:** Temperature dependence of  $\rho$  (upper figure) and S (lower figure) in the series Ag<sub>x</sub>TiS<sub>2</sub> with  $0 \leq x \leq 0.1$ .

**Figure 10:** Temperature dependence of the power factor in the series Ag<sub>x</sub>TiS<sub>2</sub> with  $0 \leq x \leq 0.1$ .

**Figure 11:** Temperature dependence of the thermal conductivity ( $\kappa$  - upper figure) and lattice contribution ( $\kappa_l$  - lower figure), in the series Ag<sub>x</sub>TiS<sub>2</sub> with  $0 \leq x \leq 0.1$ .

**Figure 12:** Temperature dependence of the figure of merit ZT in the series Ag<sub>x</sub>TiS<sub>2</sub> with  $0 \leq x \leq 0.1$ .

Table 1: Refined structural parameters for stage-2  $\text{Ag}_x\text{TiS}_2$  and stage-1  $\text{TiS}_2$ .

	<i>Samples</i>	$x = 0$	$x = 0.02$	$x = 0.05$	$x = 0.1$
Stage-1 $\text{Ag}_x\text{TiS}_2$	a (Å)	3.407(1)	3.402(1)	3.408(1)	3.408(1)
	c (Å)	5.700(1)	5.706(1)	5.710(1)	5.717(1)
	Ti (0, 0, 0) (Å) $B_{\text{iso}}$ (Å <sup>2</sup> )	0.352(1)	0.591(1)	0.712(1)	1.105(1)
	S (1/3, 2/3, z) (Å)	0.246(9)	0.244(1)	0.254(1)	0.242(1)
	$B_{\text{iso}}$ (Å <sup>2</sup> )	0.897(1)	1.341(1)	0.835(1)	0.995(1)
	$R_{\text{Bragg}}$	4.08	4.98	5.42	5.77
	$\langle \epsilon \rangle$	$6.10^{-4}$	$1.53 \cdot 10^{-3}$	$1.62 \cdot 10^{-3}$	$1.70 \cdot 10^{-3}$
$\langle \epsilon_{\text{WH}} \rangle$	$5.10^{-4}$	$1.35 \cdot 10^{-3}$	$1.43 \cdot 10^{-3}$	$1.49 \cdot 10^{-3}$	
Stage-2 $\text{Ag}_x\text{TiS}_2$	a (Å)		3.406(1)	3.409(1)	3.407(1)
	c/2 (Å)		5.766(1)	5.785(1)	5.875(1)
	Ag (0, 0, 0) (Å) $B_{\text{iso}}$ (Å <sup>2</sup> )		1.362(1)	1.423(1)	1.492(1)
	Ti (0, 0, z) (Å)		0.500	0.500	0.500
	$B_{\text{iso}}$ (Å <sup>2</sup> )		1.096(1)	1.235(1)	1.207(1)
	S1 (1/3, 2/3, z) (Å)		0.259(1)	0.263(1)	0.275(1)
	$B_{\text{iso}}$ (Å <sup>2</sup> )		0.798(0)	1.110(1)	0.996(1)
	S2 (1/3, 2/3, z) (Å)		-	-	-
	$B_{\text{iso}}$ (Å <sup>2</sup> )	-	-	-	-
$R_{\text{Bragg}}$	-	7.95	7.64	7.97	
	$\chi^2$	-	4.98	4.06	4.76
	Percentages Stage-1/ Stage-2	100% -0%	97% - 3%	95% - 5%	92% - 8%

Table 2: Refined structural parameters for  $\text{Ag}_x\text{TiS}_2$  stage-1 and stage-2 from the “ $\text{Ag}_{0.20}\text{TiS}_2$ ” pattern refinement.

$\text{Ag}_x\text{TiS}_2$ , Stage-1				
$a = 3.417(1) \text{ \AA} ; c = 6.053(1) \text{ \AA} ; \chi^2 = 3.89$				
$R_{\text{Bragg}} = 6.05 ; R_{\text{F}} = 7.24$				
	x	y	z	Biso
Ag	0.0	0.0	0.0	1.518(1)
Ti	0.0	0.0	$\frac{1}{2}$	1.549(1)
S	$\frac{1}{3}$	$\frac{2}{3}$	0.271(1)	1.319(1)
$\text{Ag}_x\text{TiS}_2$ , Stage-2				
$a = 3.416(1) \text{ \AA} ; c = 12.110(1) \text{ \AA} ; \chi^2 = 3.89$				
$R_{\text{Bragg}} = 9.00 ; R_{\text{F}} = 9.02$				
	x	y	z	Biso
Ag	0.0	0.0	0.0	0.850(1)
Ti	0.0	0.0	0.266(1)	0.749(1)
S1	$\frac{1}{3}$	$\frac{2}{3}$	0.147(1)	1.192(1)
S2	$\frac{2}{3}$	$\frac{1}{3}$	0.388(1)	0.249(1)



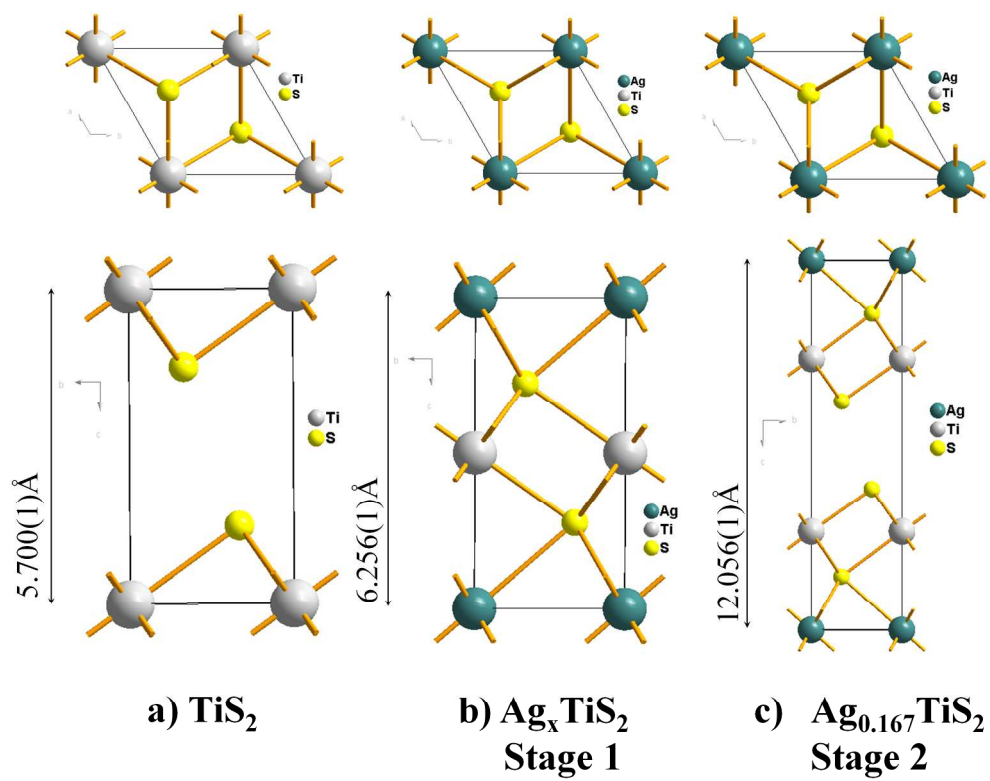


Figure 1

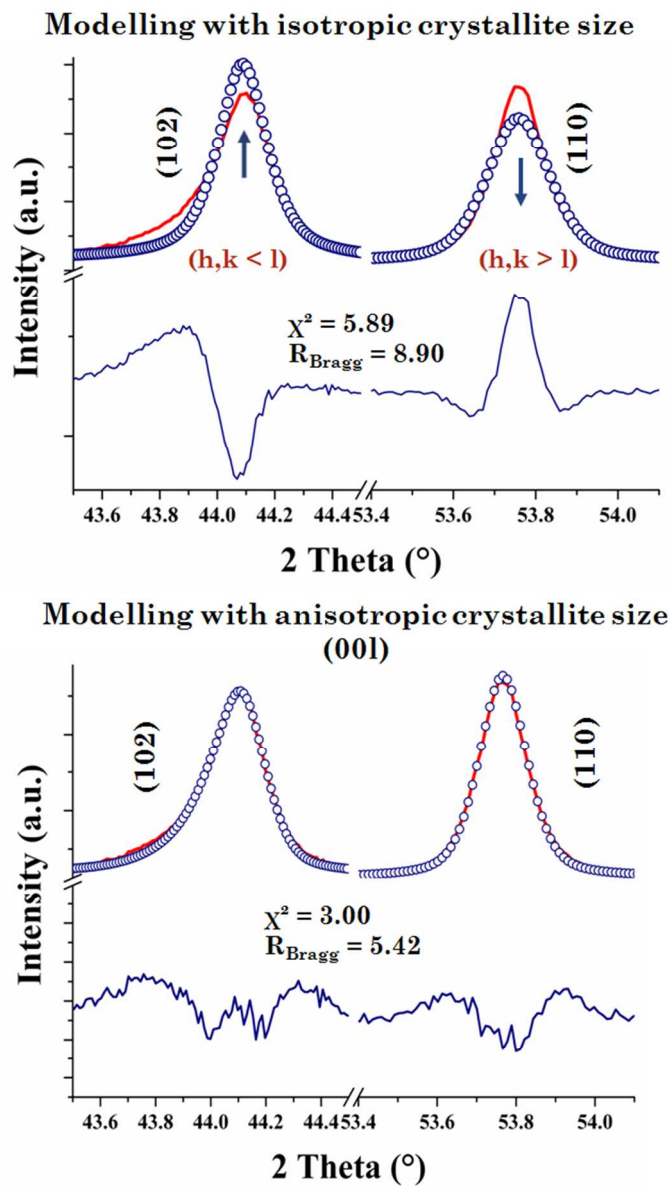


Figure 2  
172x297mm (96 x 96 DPI)

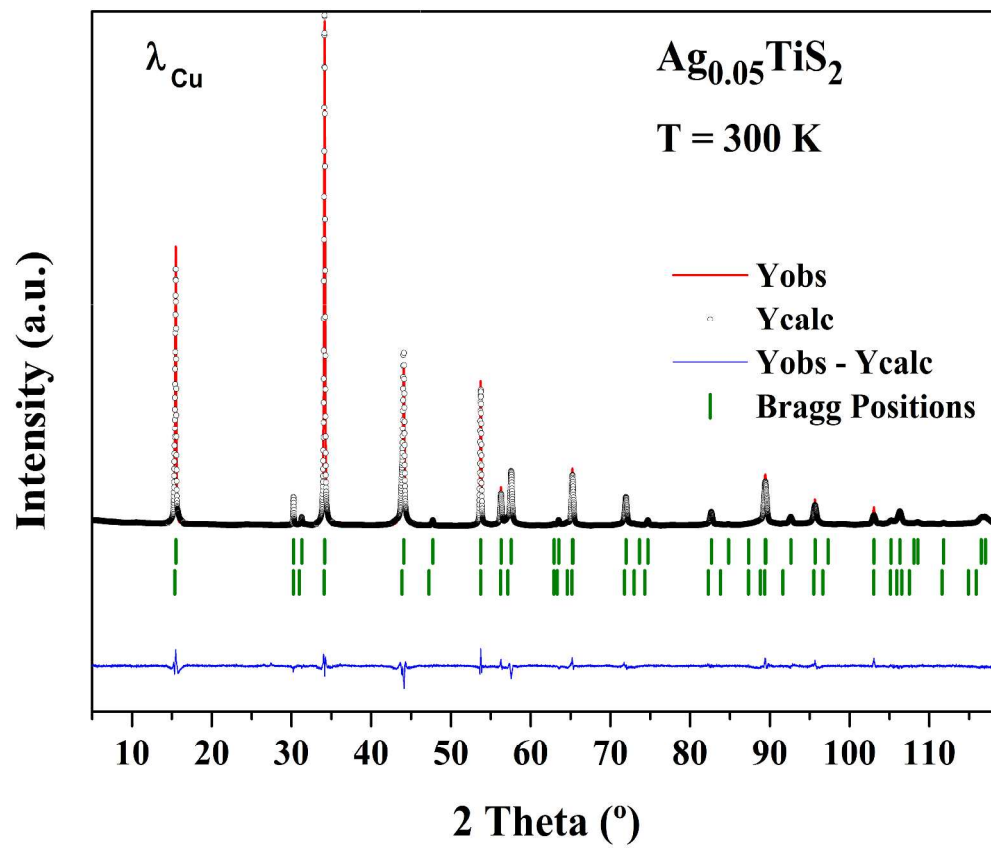


Figure 3

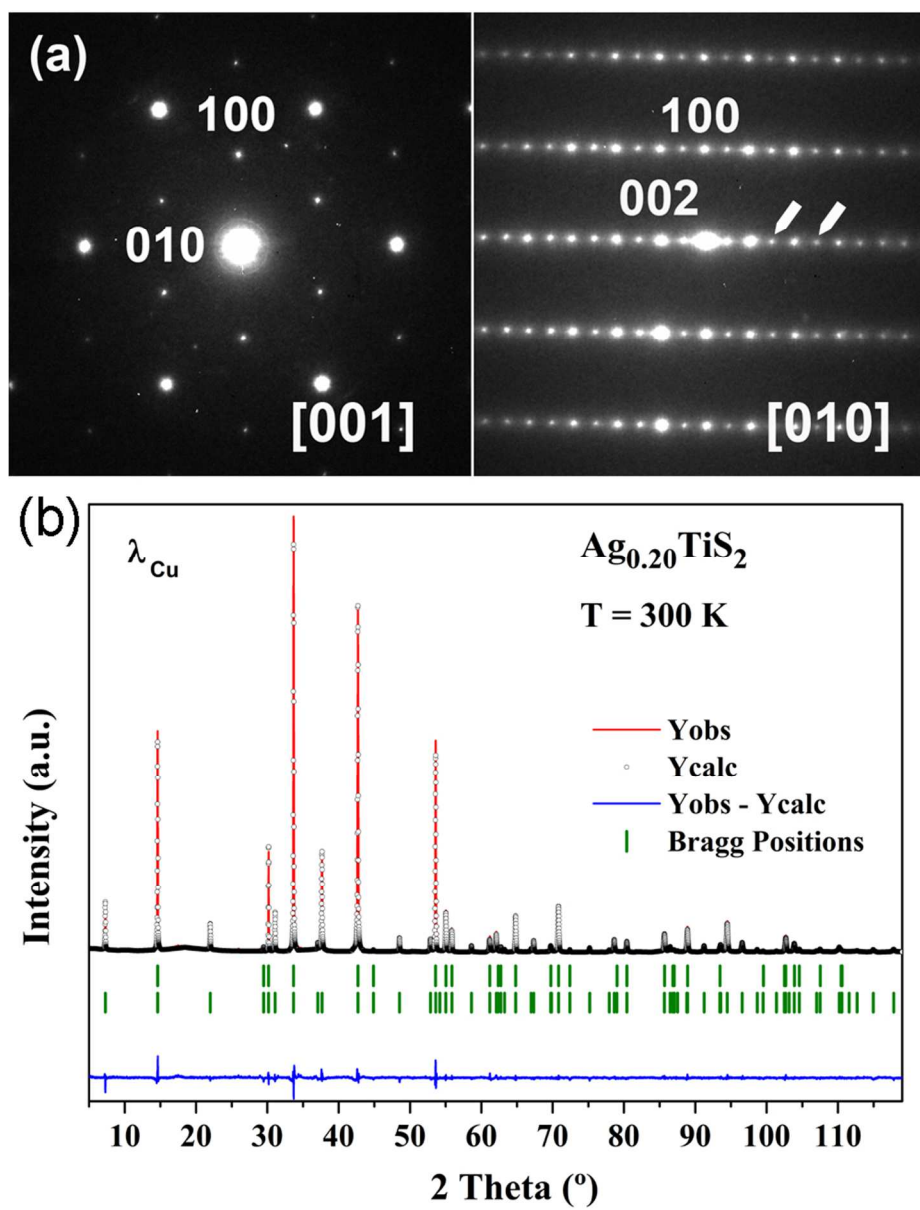


Figure 4

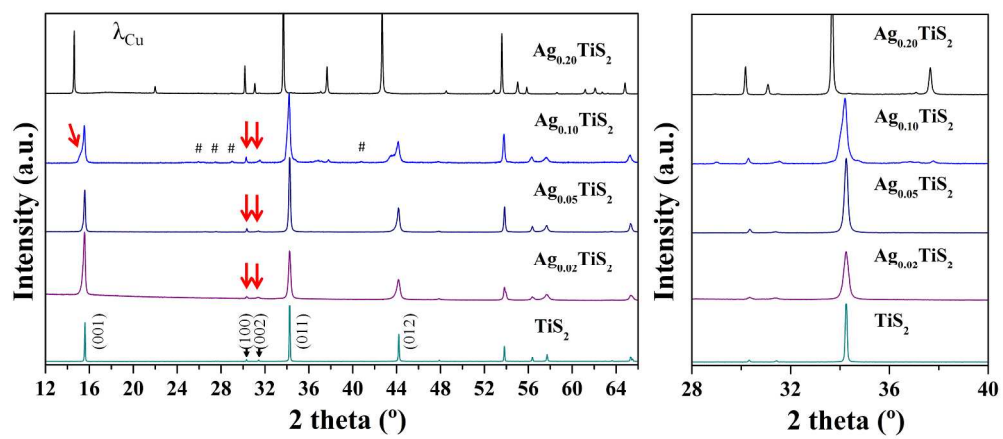


Figure 5

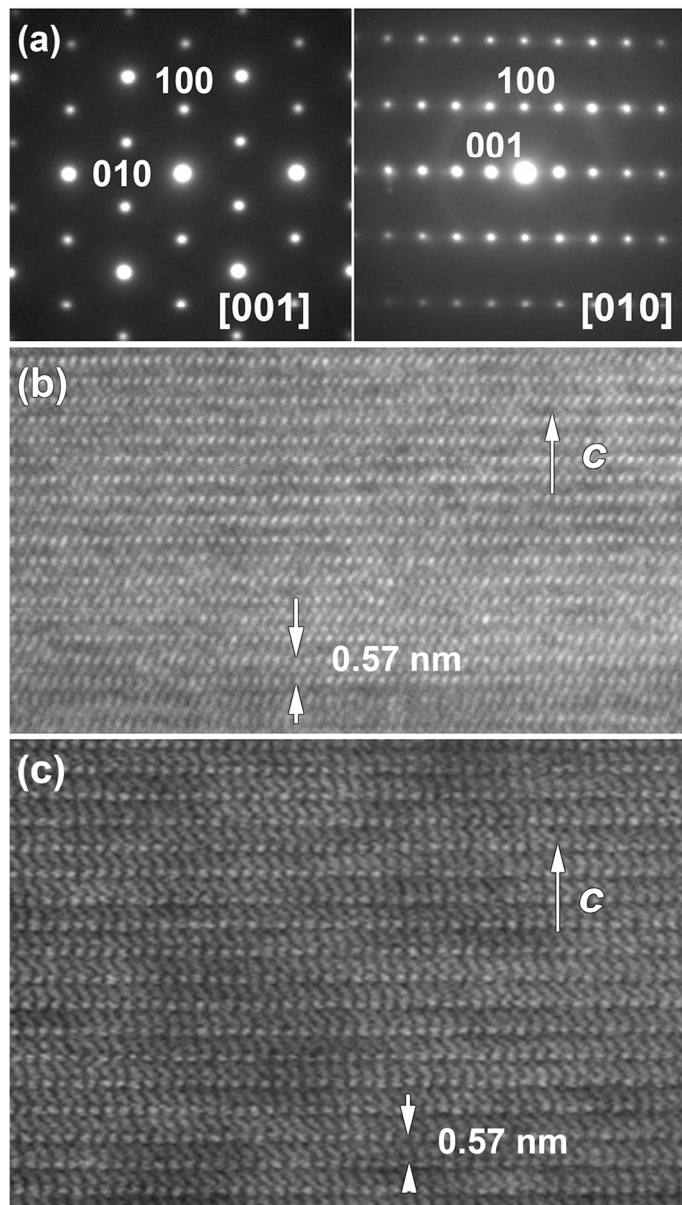


Figure 6  
96x170mm (300 x 300 DPI)

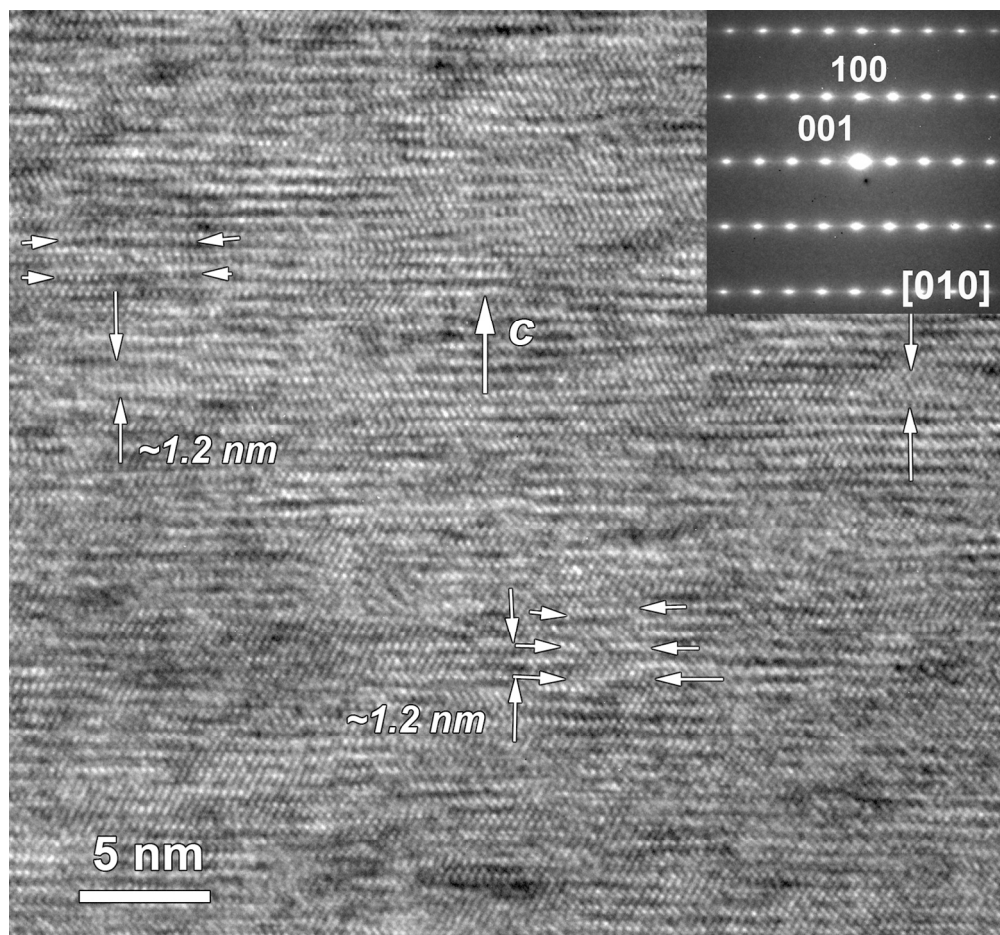


Figure 7  
132x123mm (300 x 300 DPI)

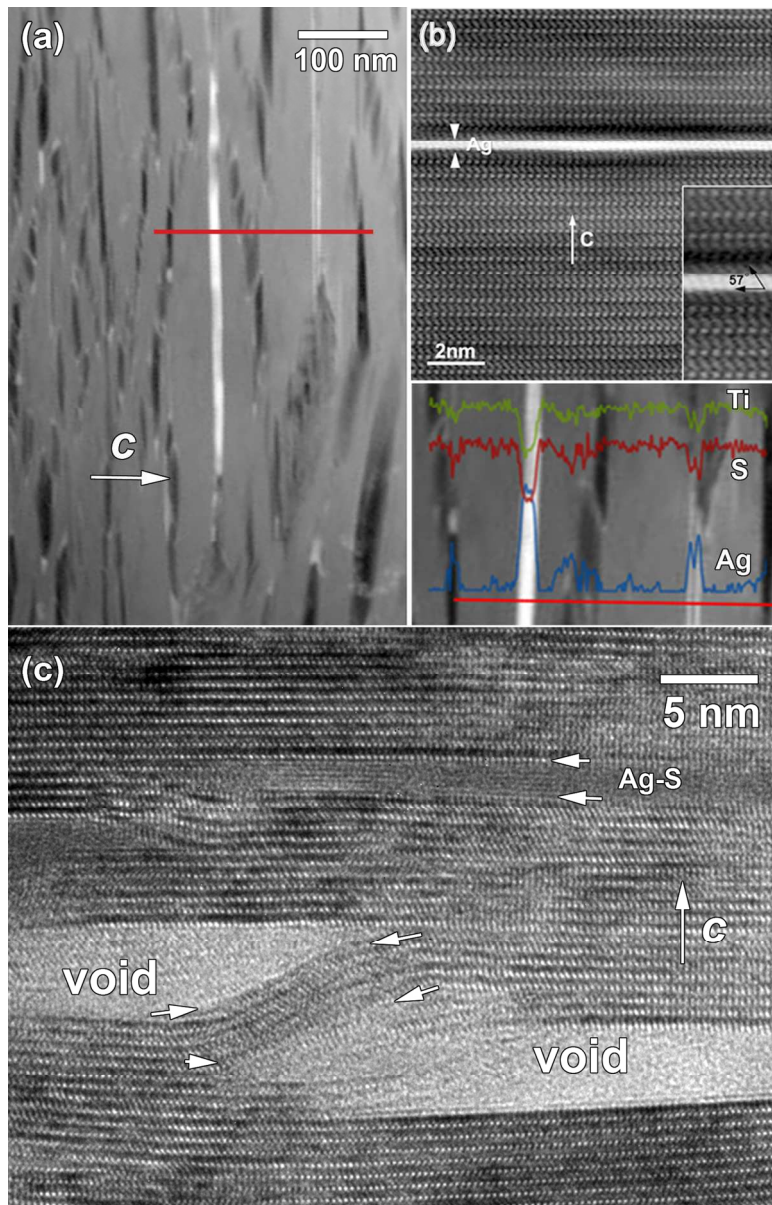


Figure 8  
129x201mm (300 x 300 DPI)

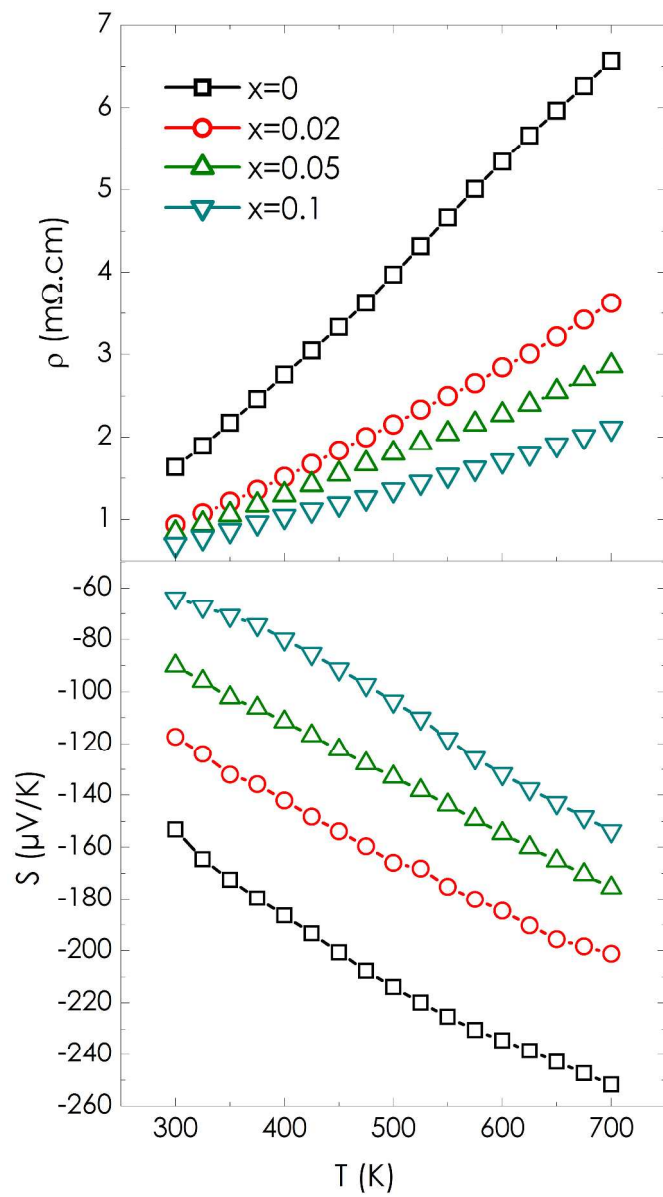


Figure 9

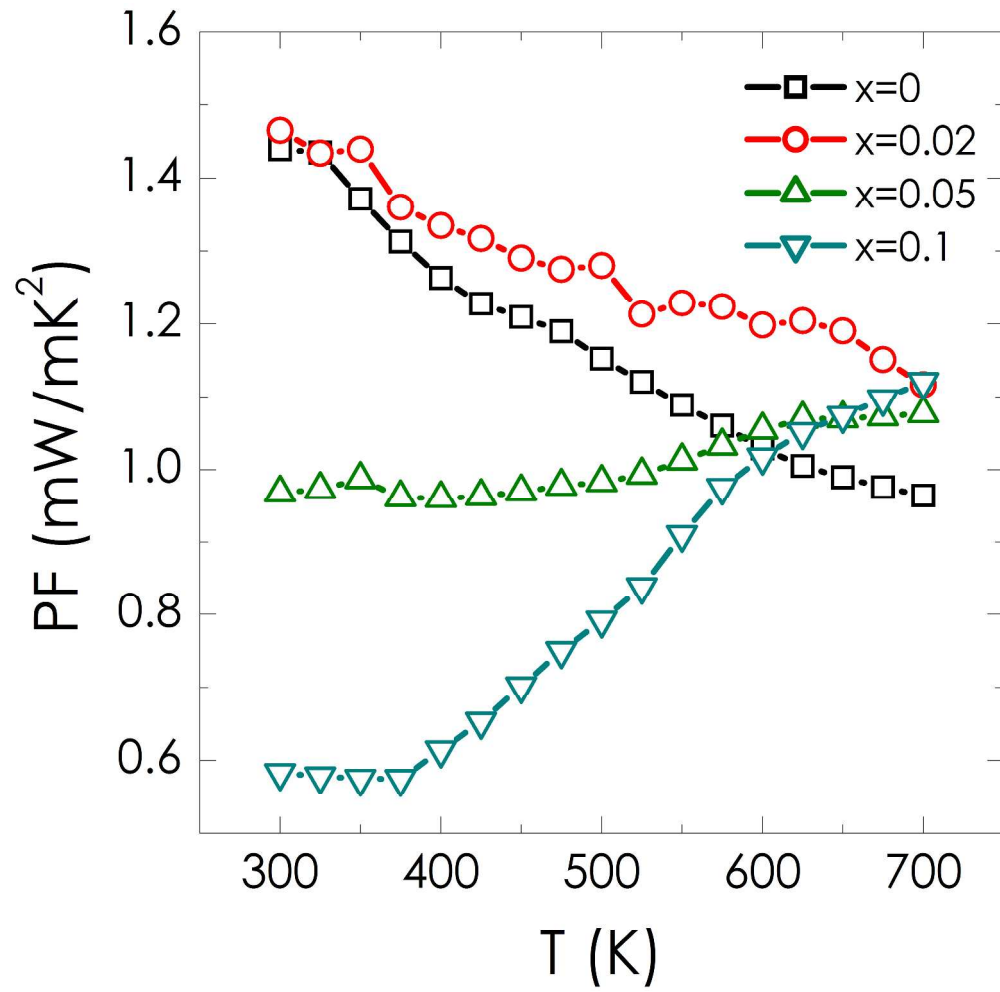


Figure 10

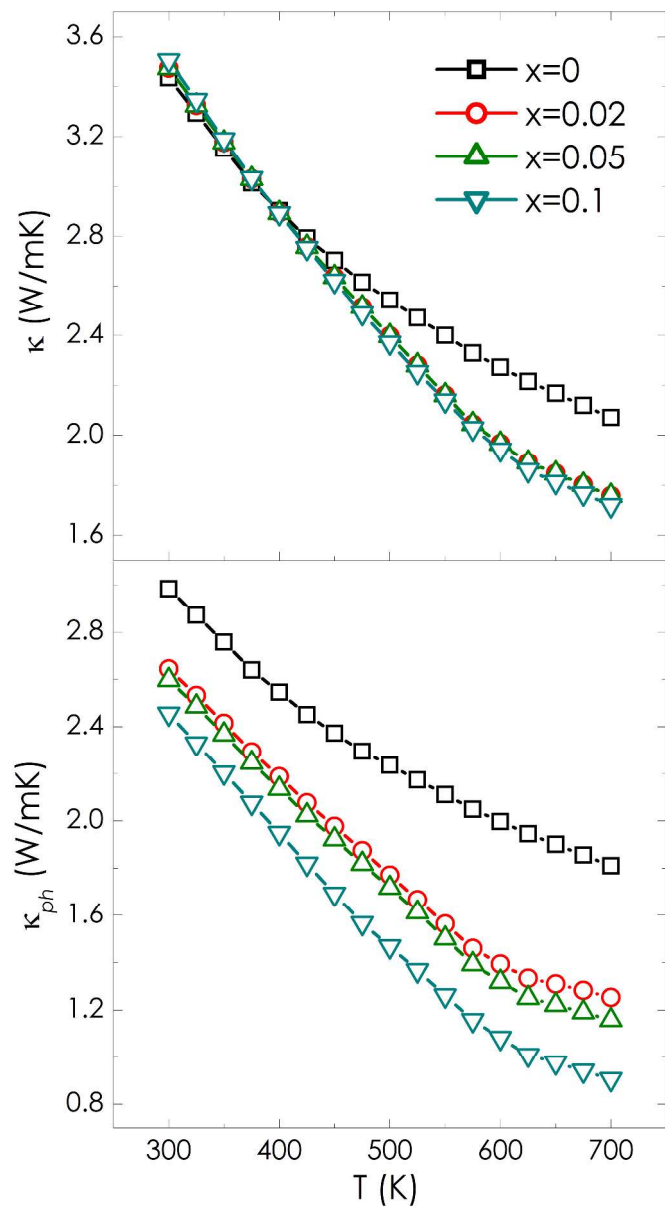


Figure 11

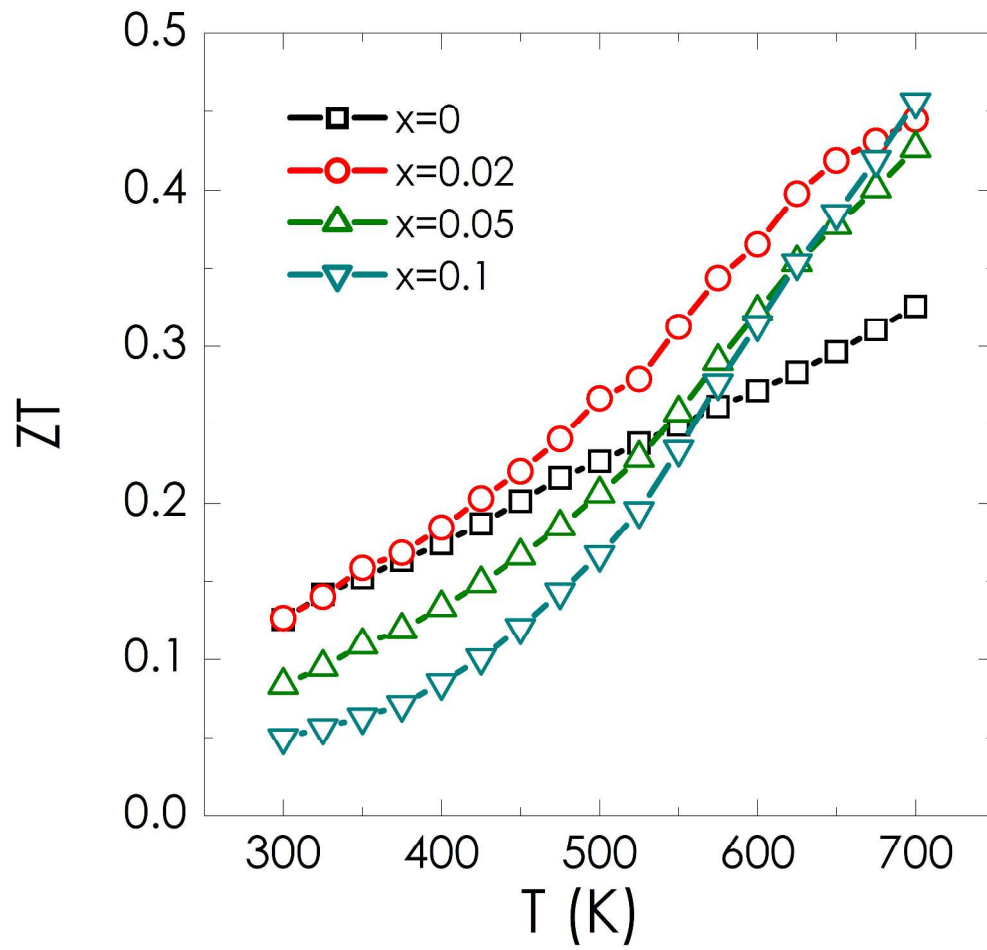


Figure 12